

Biopolymer Xanthan Gum as Promising Template for Facile Synthesis of Cerium Oxide Nanoparticles and Application as Reusable Catalyst for Reduction of Nitroaromatic Compounds

Arshpreet Kaur (✉ arshdhindsa225@gmail.com)

Sant Longowal Institute of Engineering and Technology <https://orcid.org/0000-0002-0636-381X>

Bharat Bajaj

Panjab University

Dhiraj Sud

Sant Longowal Institute of Engineering and Technology

Research Article

Keywords: Template, Cerium oxide nanoparticles, Xanthan gum, Catalyst, Reduction

Posted Date: July 20th, 2021

DOI: <https://doi.org/10.21203/rs.3.rs-711276/v1>

License: © ⓘ This work is licensed under a Creative Commons Attribution 4.0 International License.

[Read Full License](#)

Abstract

Herein, we report first time the biopolymer xanthan gum as template for facile synthesis of cerium oxide (CeO_2) nanoparticles via co-precipitation method using ultrasonication technique. The formation of nanosized particles of CeO_2 in the range of 11-32 nm with précised size and shape, as evidenced from morphological analysis. Further the polymer xanthan gum offers a versatile platform to control the morphological features and thereby the catalytic activity of CeO_2 . The prominent peaks in X-ray photoelectron spectroscopy at 82.50, 889.10, 898.50, 900.90, 907.50, and 916.60 eV binding energies confirmed the presence of Ce^{4+} in CeO_2 with no traces of template material. The significant catalytic activity of CeO_2 for the reduction of nitroaromatic compounds was observed with pseudo first order rate constants 0.1118 and 0.3318 min^{-1} for nitrobenzene and 2-nitrophenol respectively. The remarkable stability and high performance of CeO_2 were demonstrated even after four catalytic runs for nitrobenzene, affirmed the catalytic support potential of CeO_2 for reduction of nitroaromatic compounds.

1. Introduction

Nanostructured metal-based oxides gained considerable attention on the research front due to their practical applications in catalysis [1], biomedical field [2], optoelectronics [3], etc as compared to their counterparts. Substantially, research on the fabrication of nano sized metal oxides having fine shape, uniform morphology, well-defined crystal structure, and phenomenal catalytic properties has become a current hotspot. For the synthesis of metal oxide nanomaterials, one of the two approaches viz. top-down approach and bottom-up approach has been followed. The bottom-up approach provides the assembling of small atoms or molecules by operating physical/chemical forces to get the mesoporous product of high crystallinity [4, 5]. Of various synthetic routes such as templating, combustion, cathodic corrosion, aerogel formation, etc., the template-assisted synthetic strategy is considered one of the most advanced bottom-up approaches for the fabrication of metal oxides having nanometre to micrometer size of the structural units [6]. The template-assisted synthesis is a convenient strategy unresponsive to the synthetic conditions and furnished the controlled morphology, structure, and particle size of the resultant material. Template materials are categorized into the hard template (zeolites, anodic alumina membranes, etc.) and soft templates (ammonium ions, amphophilic surfactants, ionic liquids, biopolymers, etc.). In literature, a variety of nano-sized metal oxides were synthesized using different template materials such as iron oxide nanoparticles using polysaccharide (chitosan, starch, alginate, agarose, dextran, gelatin) [7, 8], CuO nanosheets using Sodium dodecyl sulfate [9], $\text{CeO}_2\text{-ZrO}_2$ mixed oxides using N-Hexadecyl-N,N,N-trimethylammoniumbromide [10], Mn_3O_4 nanoparticles using 1-*n*-butyl-3-methylimidazolium chloride and 1-*n*-butyl-3-methylimidazolium bromide [11], Co_3O_4 hollow nanostructures using Co-based zeolitic imidazolate framework (ZIF-67) [12], SnO_2 nanotubes using anodized aluminium oxide [13], etc.

Cerium, one of the most abundant rare earth metals belonging to lanthanides possesses a strong oxidation/reduction behavior during cycling between + 3 and + 4 ionic states of cerium, by virtue of the

presence of ground-state electron in 4f orbital [14]. Pure ceria exhibits a fluorite structure having some defects rely on the intrinsic property i.e., partial pressure of oxygen. The synthesis of nanostructured CeO₂ having controlled shape and size, uniform morphology, significant crystallinity with pure phase and desired composition is an indispensable attribute for their performance. The assorted synthetic methodologies such as template-assisted [15–17], flame spray pyrolysis [18, 19], reversed microemulsion method [20], hydrothermal [21–22], wet chemical [23], rapid precipitation [24], co-precipitation [25], solvothermal [26, 27], sonochemical [28], microwave [29], sol-gel [30], etc. have been employed for the synthesis of well-defined CeO₂ nanostructures. The curtailment of the size of the ceria to the nanometre range resulted in their high bandgap and significant catalytic properties. Nanostructured CeO₂ possesses the plethora of applications such as polishing agents [31], sunscreens [32], solid electrolytes [33], catalysis [34], ultraviolet absorber [35, 36], fuel additives [37], electrochemistry [38], etc. Among the various applications, catalytic performance heavily reliant upon the surface to volume ratio, oxygen storage capacity, particle size, and morphology of the ceria nanostructures [39–41]. CeO₂ is a significant redox catalyst and the relatively few literature reports exemplify the remarkable catalytic efficiency of CeO₂ nanostructures [42–46].

Xanthan gum, a high molecular weight exo-saccharide biopolymer produced by *Xanthomonas campestris* bacterium by fermentation of simple sugars. Xanthan gum is composed of pentasaccharide units that constitutes the trisaccharide chain linked with the glucose moiety. The trisaccharide chain consists of two units of mannose (α -mannose and β -mannose) and a single unit of glucuronic acid (Fig. 1). Xanthan gum is a highly stable biopolymer and the high stability is attributed to the formation of a double-helical structure [47]. Xanthan gum is comprised of several functional moieties such as primary and secondary alcohols, ester, carboxylic acid, acetate and pyruvate groups, etc.

Xanthan gum is employed in chemical sensing [48], agriculture [49], wastewater treatment [50], pharmaceuticals [51], etc. owing to their unique properties viz. high viscosity at low concentrations, biodegradability, non-toxicity, biocompatibility, etc. Additionally, xanthan gum is exploited as base fluid [52], capping agent [53], stabilizing agent [54], flocculant [55], polymerization agent [56], for the synthesis of metal oxide nanostructures. Xanthan gum can act as the template by providing favourable sites for the growth of the particles in a controlled manner and prohibited their extensive growth due to the presence of different polar functional moieties such as carboxylic group, ester group, and primary and secondary hydroxyl groups. The polar functionalities of the template interact with the particle surface consequently impact the size and shape of the particle. The particle formation process is remarkably influenced by template via controlling the nucleation and growth of nanoparticles during the oxide crystallization process. In the present study, we report the adequate and economical template-assisted synthetic methodology for the fabrication of CeO₂ nanostructures and its catalytic response for the reduction of nitroaromatic compounds. The preparation of nanoparticles has been carried out using a template-assisted sonication synthetic strategy by employing a biopolymer, xanthan gum as a template. The authors do not find any reported data in the literature related to the exploitation of xanthan gum as a

template for the synthesis of nanosized metal oxides. We have first time employed and reported the xanthan gum as a template for nanostructured CeO₂ synthesis.

The synthesized nanosized CeO₂ has the potential to be applied as catalytic support for reduction reactions. Here, we report the utilization of CeO₂ nanoparticles for the reduction of two nitroaromatic compounds viz. nitrobenzene and 2-nitrophenol as the nitro compounds are suspected to be carcinogenic and high-risk chemical. Presently, the nitroaromatic compounds are one of the largest and most important groups acting as a reactant or the intermediate for the production of drugs, synthetic dyes, pesticides, etc., and also formed as by-products during chemical reactions on the industrial level [57]. Exposure of a high concentration of nitroaromatic compounds from industrial waste to the water system causes many toxic effects on human as well as aquatic lives [58]. So, the reduction of nitroaromatic compounds viz. nitrobenzene and 2-nitrophenol to the amines is a major issue from the environmental point of view. It was investigated that merely sodium borohydride does not lead to nitro compounds reduction under ordinary reaction conditions [59, 60]. So, the combination of sodium borohydride with a catalytic amount of metal oxides Cu₂O/NaBH₄ [61], titania-supported gold catalyst/NaBH₄ [62], Co₃O₄/NaBH₄ [63], CuO/γ-Al₂O₃/NaBH₄ [64], reduced graphene oxide-ZnO/NaBH₄ [65], multiple Au cores in CeO₂/NaBH₄ [42], etc. in the protic or aqueous solvent system has been adopted results to the reduction reactions.

2. Experimental

2.1 Chemicals

Xanthan gum and ceric ammonium nitrate was obtained from SD Fine-Chem. Limited. For catalytic reactions, nitrobenzene was purchased from Avantor Performance Materials India Limited and 2-nitrophenol was acquired from Alfa Aesar. Solvents ethanol and methanol used were of analytical grade. All the synthesis reactions were carried out using deionized water.

2.2 Synthesis of template-assisted CeO₂ nanoparticles

In a typical procedure, CeO₂ nanoparticles have been prepared using biopolymer xanthan gum as a template via template-assisted co-precipitation method as shown in Fig. 2. The synthesis was carried out by the following route: xanthan gum solution (0.25%) was prepared by dissolving xanthan gum in 20 mL deionized water under moderate stirring for 1 hour. The aqueous solution of ceric ammonium nitrate (0.5 M) was added to the xanthan gum solution followed by stirring for 2 hours. The resultant solution was precipitated with ammonium hydroxide under continuous stirring for 3 hours. The reaction mixture was kept in probe ultrasonicator and exposed to sound waves for 30 min at 50°C. The precipitates were filtered by vacuum filtration, washed 3–4 times with deionized water, and dried in a hot air oven at 80°C for 3 hours. Any traces of xanthan gum left were removed during the calcination of pale-yellow coloured precipitates and the final product was obtained.

The synthesis procedure of template-assisted CeO₂ nanoparticles was optimized by varying the several reaction parameters: (a) calcination temperature, (b) reaction time, and (c) pre-treatment time of template material. The impact of variation of reaction parameters was by change in crystallinity, morphology, particle size, and shape of the synthesized nanoparticles. The influence of the size of xanthan gum particles on the morphology of the synthesized nanoparticles was also investigated by sonicating the xanthan gum for different time intervals.

2.3 Characterization

The morphology of CeO₂ nanoparticles was investigated by FE-SEM (JSM-7610Plus JEOL) at an accelerating voltage of 10–15 kV and HR-TEM (Tecnai 200 kV TEM) Fei, electron optics. Furthermore, formation of CeO₂ nanoparticles was confirmed through EDS measurement. The crystal phase and crystal structure identification of synthesized product was carried out on X-ray diffractometer D8 Advance Bruker employing Cu Ka radiation (= 1.54060 Ang) having a scanning rate of 5° per min in the 2θ angle ranged from 5° to 100°. The thermogravimetric curve was recorded on the Thermogravimetric analyzer TGA-4000 (Perkin Elmer) to check the stability of the sample. The chemical state and composition of CeO₂ nanoparticles was recognized using X-ray photoelectron spectroscopy (Thermofisher scientific, Nexsa base). The UV-Vis absorption spectra were recorded using UV-Vis spectrophotometer (UV-1800, Shimadzu) for tracking the path of the reduction reaction. The IR spectrum was recorded on a Fourier Transform infrared spectrometer (Spectrum RX-IFTIR, Perkin Elmer) for the confirmation of formation of end products of the reduction reaction.

3. Results And Discussion

The preparation of CeO₂ nanoparticles was attained through the template-assisted route using biopolymer xanthan gum as a template. The synthesis of nanosized CeO₂ was carried out using ceric ammonium nitrate as a precursor and ammonium hydroxide as a precipitating agent. Reaction scheme 1 represents the steps involved in the synthesis of CeO₂. The ceric ammonium nitrate is converted to cerium hydroxide in the presence of a base (ammonium hydroxide) which was precipitated out and calcined at various temperatures. The calcination of the as-synthesized sample led to the formation of cerium (III) oxide.

1. Field emission scanning electron microscopy (FESEM) and powder X-ray diffraction (XRD) analysis of template-assisted CeO₂ nanoparticles

The parameters for the synthesis of CeO₂ nanoparticles has been optimized by varying the calcination temperature, period of the reaction, pre-treatment has given to the template and the impact of these parameters was evaluated in terms of influence on the morphology, shape, and average crystallite size of the CeO₂ nanoparticles as evidenced by FESEM and XRD analysis.

3.1.1 Effect of calcination temperature

The effect of calcination was scrutinized by calcinating the as-synthesized sample at different temperatures viz. 350°C, 500°C, 650°C and 800°C and obtained CeO₂ nanoparticles was named as C-350, C-500, C-650, and C-800 respectively. FESEM images shown in Fig. 3 demonstrate the increase in uniformity in shape and size of CeO₂ nanoparticles with an increase in calcination temperature. The calcination of the sample at 650°C leads to a more regular surface.

The effect of calcination temperature on the crystallinity of the CeO₂ nanoparticles was manifested by a non-destructive, analytical tool i.e., Powder XRD analysis. The influence of calcination temperatures viz. 350°C, 500°C, 650°C and 800°C on crystal structure and phase of template induced CeO₂ nanoparticles was investigated. The XRD patterns of the sample C-650 showed strong and intense diffraction peaks as compared to C-350, C-500, and C-800. The diffraction peaks at 28.4, 32.976, 47.363, 56.223, 59.026, 69.364, 76.651, 79.036 and 88.387 correspond to (1 1 1), (2 0 0), (2 2 0), (3 1 1), (2 2 2), (4 0 0), (3 3 1), (4 2 0) and (4 2 2) planes of CeO₂, space group Fm3m (2 2 5), edge length (a = b = c) = 5.42800 and volume of unit cell 159.93 indexing the cubic fluorite crystal structure/phase of C-350, C-500, and C-800. The observed patterns of samples were matched with JCPDS card numbers 00-043-1002, 01-075-8371, 00-067-0122, 00-034-0394 respectively. The data depicts that calcination temperature has no effect on the crystal structure and phase of the template-assisted CeO₂ nanoparticles. However, with an increase in calcination temperature, the amorphous nature of the sample changes into the highly crystalline state as shown in Fig. 4. At 650°C, the nanostructured CeO₂ shows high crystallinity and beyond which peak intensity gets diminished. The perfect coincidence with CeO₂ and no other diffraction peak observed other than the CeO₂ delineated the purity and high crystallinity of the product. The average crystallite size of the CeO₂ calcined at 650°C was appraised to be 61 nm using the Debye Scherrer equation.

$$D = 0.9 \lambda / \beta \cos \theta$$

Where D = Average particle size

B = Full Width at Half Maxima (FWHM)

θ = Bragg's angle

λ = Wavelength of CuK α radiations

Based on FESEM and XRD analysis of calcinated CeO₂ nanoparticles, further investigations were performed using C-650.

3.1.2 Effect of reaction time

To determine the effect of reaction time on the surface morphology of the template-assisted CeO₂ nanoparticles, the synthetic reactions have been carried out by varying the reaction time from 10–50 min. The surface analysis of the CeO₂ synthesized at the different time period (shown in Fig. 5) depicts that reaction carried out for 10 min (Fig. 5(a)) resulted in the irregular and non-uniform morphology of the

particles. The particle distribution tends to uniformity with improvement in shape and size of the particles by increasing the reaction time up to 30 min as shown in Fig. 5(e). The further increment in reaction time led to the uneven distribution of the particles and enlargement which resulted in the irregular morphological structures.

3.1.3 Effect of pre-treatment of xanthan gum

The morphology and size of the template material strongly influence the shape and size of the nanoparticles [66]. The same observation has been noticed in xanthan gum-assisted CeO_2 nanoparticles as revealed by FESEM images. For comparative studies, template-free synthesis of CeO_2 nanoparticles has also been carried out and morphological features of template-free CeO_2 have been shown in Fig. 6(a). The FESEM images of xanthan gum (Fig. 6(b-1)) has larger particle having the size in micrometres and possesses irregular morphology and the synthesized CeO_2 (Fig. 6(b-2)) also depicts the similar characteristics such as non-uniformity particles with size in the micrometre range. In order to prepare the nanosized CeO_2 , an attempt has been delivered to reduce the size of template particles by its pre-treatment through the ultrasonication process. Thus, ultrasonication was used as a tool for reduction of the size of template material and xanthan gum by exposing xanthan gum to sound waves of 40 kHz for different time intervals viz. 20 min, 40 min, and 60 min to acquire the CeO_2 particles in the nano range, and the obtained CeO_2 nanoparticles are denoted as C-20, C-40, and C-60 respectively. The FESEM images of xanthan gum treated for 40 min and the subsequently synthesized CeO_2 nanoparticles are shown in Fig. 6(c-1) and 6(c-2) respectively. The morphological analysis thus supported the significant effect of pre-sonication of the template on the CeO_2 nanoparticle morphology.

Further, from FESEM results represented in Fig. 7, it was investigated that sonication of xanthan gum for 20 min has not much effect on the morphology and manifested the non-uniformity and irregularity in shape and size of the nanoparticles whereas 60 min sonication led to agglomeration of nanoparticles as the particles get adhered to each other through the grain boundary. However, 40 min sonication of xanthan gum was optimized condition selected for synthesis of CeO_2 nanoparticles having uniform surface as well as well-defined shape and size. Figure 7(d) represents the EDS spectra and conveys the information about the elemental composition of the synthesized CeO_2 nanoparticles.

The XRD data of as-synthesized CeO_2 nanoparticles C-20, C-40, and C-60 was recorded and presented in Fig. 8. Powder XRD analysis manifested the crystalline nature of CeO_2 with no change in crystal phase and structure. It has been observed the pre-treated xanthan gum used as a template greatly influences the size of the CeO_2 nanoparticles by reducing the size to half of the nanoparticles prepared by using untreated xanthan gum. The calculated average crystallite size, dislocation density, and lattice strain of the C-20, C-40, and C-60 nanoparticles has been shown in the Table 1. During synthesis, some defects and strain to the lattice occur attributed to the crystal imperfections. The dislocation density and lattice strain are calculated using equations [67],

Table 1
The average crystallite size, dislocation density and lattice strain of C-20, C-40 and C-60 CeO₂ nanoparticles

Sample	Average crystallite size (nm)	Dislocation density (nm ⁻²)	Lattice strain
C-20	39	0.000883673	0.000648727
C-40	30	0.001226587	0.000493421
C-60	37	0.000905511	0.000619197

Dislocation density = $1/D^2$

Lattice strain = $\beta/4\tan\theta$

3.2 High-resolution transmission electron microscopy (HRTEM) analysis

The nanoparticle size of CeO₂ (C-40) was evaluated from HTREM images obtained at different magnifications which have been shown in Fig. 9. The even distribution of nanoparticles having spherical morphology and a slight tendency of agglomeration was noticed. The particle size has been found in the range of 11–32 nm which is also in good agreement with average crystallite size as obtained from XRD data.

3.3 X-ray photoelectron spectroscopy analysis

For the characterization of the chemical state of cerium in synthesized CeO₂ nanoparticles, XPS analysis was carried out (shown in Fig. 10). The peak at 917 eV (satellite peak) clearly indicated the +4 valence state or tetravalent Ce in CeO₂ as this peak is absent in the case of Ce³⁺. The 6 characteristic peaks in the spectra corresponding to binding energies 882.50, 889.10, 898.50, 900.90, 907.50, and 916.60 eV clearly depict the complete oxidation of Ce³⁺ to Ce⁴⁺. The final electronic states of cerium – 3d⁹ 4f⁰ and oxygen - p⁶ results in the peaks corresponding to highest binding energies viz. 898.50 and 916.60 eV. The peaks corresponding to lower binding energies viz. 882.50, 900.90, eV is due to the 3d⁹ 4f² electronic state of cerium and 2p⁴ of oxygen and the peaks at binding energies 889.10 and 907.50 are the result of 3d⁹ 4f¹ and 2p⁵ electronic states of cerium and oxygen.

3.4 Thermogravimetric analysis (TGA)

Thermogravimetric analysis has investigated the thermal stability of the CeO₂ nanoparticles by detecting the change in weight % with the variation in time and temperature under controlled atmospheric conditions. The TGA data showed only 2% weight loss of the CeO₂ nanoparticles in the temperature range 25°C to 800°C which confirmed the high stability of synthesized nano-size CeO₂.

1. Evaluation of catalytic efficiency of CeO₂ for the reduction of nitroaromatic compounds

The catalytic activity of CeO₂ nanoparticles was studied for the reduction of nitroaromatic compounds. Nitrobenzene and 2-nitrophenol were chosen as model compounds for the catalytic reduction process using sodium borohydride (NaBH₄) as a reducing agent. Scheme 2 represents the catalytic reduction of nitrobenzene and 2-nitrophenol. First, for the reduction of nitrobenzene, 0.2 mmol sodium borohydride was added to 2 X 10⁻⁴ mol/L solution of nitrobenzene and the mixture was stirred for 1–2 min, followed by the addition of CeO₂ nanoparticles (10 mg) to the reaction mixture and moderately stirred till completion of the reaction. Similarly, the catalytic reduction of 2-nitrophenol has been carried out. The reaction progress was monitored via a UV-vis spectrophotometer.

The UV-vis spectra of the aqueous solution of nitrobenzene showed a characteristic peak at 258 nm and the hypochromic shift or decrease in absorption of nitrobenzene with the appearance of the band at 236 nm (shown in Fig. 11) evidenced the formation of product within reaction time 10 min. A similar procedure was adopted for the reduction of 2-nitrophenol. The reactant was converted to 2-aminophenol with a 2 min reaction time as monitored via UV-vis spectrophotometer. The confirmation of completion of the reaction was confirmed from TLC, UV-vis spectral analysis, FTIR spectroscopy.

The FT-IR spectra of end products of deduction reactions i.e aminobenzene and 2-aminophenol are presented in Fig. 12. The FT-IR spectrum of aminobenzene showed a characteristic peak at 3350–3427 cm⁻¹ owing to the N-H stretching vibrations of the aromatic amine group. The vibrational modes of C-H stretching were observed at 3033 cm⁻¹. The vibration peak for -NH bending was observed at 1618 cm⁻¹ and C-C and C-N stretching vibrations were observed at frequency 1496 and 1272 cm⁻¹ respectively.

In the FT-IR spectrum of 2-aminophenol, the characteristic peak at 3304–3375 cm⁻¹ was due to the hydrogen bonded -OH stretch and -NH stretch of the amine group. The vibrational peak at 2989–3022 cm⁻¹ was due to the -CH stretching. The peaks for and C = C stretching and -NH bending vibrations were observed at 1602 cm⁻¹. The C-C and C-N stretch showed the vibrational mode at absorption peaks at 1511 and 1267 cm⁻¹ respectively. The peak at 1029–1080 cm⁻¹ represents the stretching vibrations of the C-O bond. The absence of peak corresponding to nitro group further validated the conversion to the amino group.

4.1 Kinetics of reduction of nitroaromatic compounds

In the catalytic reduction of nitroaromatic compounds, the high concentration of sodium borohydride endorsed the reaction to follow pseudo first-order kinetics of the reaction, thereupon the rate of reaction relies upon the concentration of reactant i.e., nitrobenzene and 2-nitrophenol. The rate of reaction for pseudo first-order reaction can be calculated from the slope by plotting a graph between ln(A_t/A₀) and time (t) for catalytic reduction (shown in Fig. 13) by using an equation

$$\ln(A_t/A_0) = -kt$$

where, A_t = Absorbance at time t

A_0 = Absorbance at time $t = 0$

k = rate constant

t = time of the reaction

The plot of $\ln(A_t/A_0)$ versus time (min) divulges a straight line with a negative slope which represents the rate constant (k). From this plot, the rate constants for reduction of nitrobenzene (in the presence and absence of catalyst) were found to be 0.118 min^{-1} and 0.0179 min^{-1} with correlation coefficient (R^2) value of 0.991 and 0.994. The observed rate constant values for 2-nitrophenol (in the presence and absence of catalyst) were 0.3318 min^{-1} and 0.0156 min^{-1} with R^2 values of 0.98 and 0.88. An attempt has been made to compare the pseudo first-order rate constants and reaction time obtained in the current study with the data in the literature for the reduction reaction of nitroaromatic compounds using CeO_2 nanoparticles and other nanomaterials (Table 2).

Table 2

Comparison of reaction time and rate constant data of reduction of nitro compounds published in literature with the present work

Catalyst	Nitro compound	Reaction time (min)	Rate constant (min^{-1})	Ref.
CeO ₂ nanoparticles	Nitrobenzene	80	-	[68]
Copper nanoparticles	o-nitrophenol	18 min	0.092	[69]
BiO(OH)/activated carbon	Nitrobenzene	120	-	[70]
Bi ₂ MoO ₆	Nitrobenzene	20	-	[71]
zero-valent iron	Nitrobenzene	240	0.0006	[72]
Au-(N-isopropylacrylamide) nanoparticles	Nitrobenzene	-	0.00432	[73]
Alginate-Silver Nanoparticles	Nitrobenzene	8	0.31	[74]
Pd nanoparticles/reduced graphene oxide	Nitrobenzene	55	-	[75]
Gold nanoparticles	2-nitrophenol	-	0.004638	[76]
Gold nanoparticles	2-nitrophenol	5	-	[77]
Cu ₂ O/reduced graphene oxide	2-nitrophenol	5	1.64	[78]
CeO ₂ nanoparticles	Nitrobenzene	10	0.1118	Present work
	2-nitrophenol	2	0.3318	Present work

4.2 Reusability of catalyst

The reusability of the catalyst was tested by conducting four catalytic cycles for the reduction of nitrobenzene. The reduction reaction was carried out by adding 0.2 mmol sodium borohydride and 10 mg catalyst to the 2×10^{-4} mol/L solution of nitrobenzene. After the completion of the reaction, the catalyst was recovered by filtering the reaction mixture and washed several times with ethanol, dried in a hot air oven at 80°C for 5 hours, and used for the next catalytic cycle. A similar procedure was repeated for four catalytic cycles for the reduction of nitrobenzene. The reaction profile obtained from UV-vis spectral studies for four catalytic cycles is presented in Fig. 14. From the reaction profile, it has been concluded that no observable change in completion of reaction with time was noticed and hence concluded no significant loss in the catalytic activity of CeO₂ nanoparticles even after four reusability cycles.

5. Conclusion

The present study reported the fabrication of CeO₂ nanoparticles (C-40) prepared by template-assisted co-precipitation method employing xanthan gum as a template. The précised shape and morphology were obtained by optimizing reaction parameters viz. calcination temperature, reaction time, and sonication time of template. XRD results confirmed the cubic fluorite crystal structure and highly crystalline nature of nano-sized CeO₂ having an average crystallite size of 30 nm. The X-ray photoelectron spectroscopy established the presence of cerium having a + 4 chemical state. The morphological analysis manifested the uniform and spherical morphology of the nanoparticles having a particle size in the range of 11–32 nm. Thermogravimetric analysis endorsed the stability of the CeO₂ nanoparticles which are further employed as a catalyst for the reduction of nitroaromatic compounds: nitrobenzene and 2-nitrophenol. The complete reduction of nitrobenzene and 2-nitrophenol into respective products was observed in 10 min and 2 min respectively as monitored by UV-vis spectral analysis. Further, reusability data supported the potential of synthesized CeO₂ nanoparticles as catalytic support for reduction reactions of nitroaromatic compounds with no significant loss in the catalytic activity and thereby, can decontaminate the environmental matrix.

Declarations

Acknowledgements

The authors greatly acknowledge the SLIET chemical society to provide facilities which made this work successful. We are pleased to acknowledge the facilities provided Panjab University, Chandigarh; Indian Institute of Technology Mandi, Himachal Pradesh.

Funding

This research did not receive any specific grant from funding agencies in the public, commercial, or not-for-profit sectors.

Conflict of Interest

The authors report no declarations of interest.

References

1. Singh B, Na J, Konarova M, Wakihara T, Yamauchi Y, Salomon C, Gawande MB (2020) Functional Mesoporous Silica Nanoparticles for Catalysis and Environmental Applications. *Bull Chem Soc Jpn* 93:1459–1496
2. Ahmadi A, Hosseini-Nami S, Abed Z, Beik J, Aranda-Lara L, Samadian H, Morales-Avila E (2020) Jaymand, Shakeri-Zadeh, M.: A Recent advance in ultrasound-triggered drug delivery through lipid-based nanomaterials. *Drug Discov Today* 00:2182–2200

3. Wang J, Song J, Mu X, Sun M (2020) Optoelectronic and photoelectric properties and applications of graphene-based nanostructures. *Mater Today Phys* 13:100196
4. Khalily MA, Eren H, Akbayrak S, Susapto HH, Biyikli N, Özkar S, Guler MO (2016) Facile Synthesis of Three-Dimensional Pt-TiO₂ Nano-networks: A Highly Active Catalyst for the Hydrolytic Dehydrogenation of Ammonia–Borane. *Angew Chem Int Ed* 55:1–6
5. Roy M, Ghosh S, Naskar MK (2015) Ligand-assisted soft-chemical synthesis of self-assembled different shaped mesoporous Co₃O₄: efficient visible light photocatalysts. *Phys Chem Chem Phys* 17:10160–10169
6. Poolakkand RR, Menampambath MM (2020) Soft-template-assisted synthesis: a promising approach for the fabrication of transition metal oxides. *Nanoscale Adv* 2:5015–5045
7. Nidhin M, Indumathy R, Sreeram KJ, Unni Nair B (2008) Synthesis of iron oxide nanoparticles of narrow size distribution on polysaccharide templates. *Bull Mater Sci* 31:93–96
8. Rafi MM, Ahmed KSZ, Nazeer KP, Kumar DS, Thamilselvan M (2015) Synthesis, characterization and magnetic properties of hematite (α-Fe₂O₃) nanoparticles on polysaccharide templates and their antibacterial activity. *Appl Nanosci* 5:515–520
9. Jang KS, Kim JD (2011) In Situ Catalytic Activity of CuO Nanosheets Synthesized from a Surfactant-Lamellar Template. *J Nanosci Nanotechnol* 11:4496–4500
10. Tsoncheva T, Ivanova R, Henych J, Dimitrov M, Kormunda M, Kovacheva D, Scotti N, Santo VD, Stengl V (2015) Effect of preparation procedure on the formation of nanostructured ceria–zirconia mixed oxide catalysts for ethyl acetate oxidation: Homogeneous precipitation with urea vs template-assisted hydrothermal synthesis. *Appl Catal A-Gen* 502:418–432
11. Akbari J, Heydari A (2012) Synthesis of Mn₃O₄ Nanoparticles with Controlled Morphology Using Ionic Liquid. *Curr Nanosci* 8:398–401
12. Shao J, Wan Z, Liu H, Zheng H, Gao T, Shen M, Qu Q, Zheng H (2014) Metal organic frameworks-derived Co₃O₄ hollow dodecahedrons with controllable interiors as outstanding anodes for Li storage. *J Mater Chem A* 2:12194–12200
13. Wang Y, Lee JY, Zeng HC (2005) Polycrystalline SnO₂ Nanotubes Prepared via Infiltration Casting of Nanocrystallites and Their Electrochemical Application. *Chem Mater* 17:3899–3903
14. Reed K, Cormack A, Kulkarni A, Mayton M, Sayle D, Klaessig F, Stadler B (2014) Exploring the properties and applications of nanoceria: is there still plenty of room at the bottom? *Environ Sci Nano* 1:390–405
15. Sifontes AB, Gonzalez G, Ochoa JL, Tovar LM, Zoltan T, Canizales E (2011) Chitosan as template for the synthesis of ceria nanoparticles. *Mater Res Bull* 46:1794–1799
16. Vantomme A, Yuan ZY, Du G, Su BL (2005) Surfactant-Assisted Large-Scale Preparation of Crystalline CeO₂ Nanorods. *Langmuir* 21:1132–1135
17. Liu H, Wang M, Wang Y, Liang Y, Cao W, Su Y (2011) Ionic liquid-templated synthesis of mesoporous CeO₂–TiO₂ nanoparticles and their enhanced photocatalytic activities under UV or visible light. *J Photochem Photobiol A* 223:157–164

18. Lord MS, Jung M, Teoh WY, Gunawan C, Vassie JA, Amal R, Whitelock JM (2012) Cellular uptake and reactive oxygen species modulation of cerium oxide nanoparticles in human monocyte cell line U937. *Biomaterials* 33:7915–7924
19. Xia T, Kovoichich M, Liang M, Madler L, Gilbert B, Shi H, Yeh JI, Zink JI, Nel AE (2008) Comparison of the Mechanism of Toxicity of Zinc Oxide and Cerium Oxide Nanoparticles Based on Dissolution and Oxidative Stress Properties. *ACS Nano* 2:2121–2134
20. Pournajaf R, Tabrizi SAH, Jafari M (2014) Reverse microemulsionsynthesis of CeO₂ nanopowder using polyoxyethylene(23)laurylether as a surfactant. *Ceram Int* 40:8687–8692
21. Masui T, Hirai H, Hamada R, Imanaka N, Adachi G, Sakata T, Mori H (2003) Synthesis and characterization of cerium oxide nanoparticles coated with turbostratic boron nitride. *J Mater Chem* 13:622–627
22. Masui T, Hirai H, Imanaka N, Adachi G (2002) Synthesis of cerium oxide nanoparticles by hydrothermal crystallization with citric acid. *J Mater Sci Lett* 21:489–491
23. Xua Y, Li R (2018) Wet-chemical synthesis and characterization of nitrogen-doped CeO₂ powders for oxygen storage capacity. *Appl Surf Sci* 455:997–1004
24. Kavitha P, Ramesh R, Rajan MR, Stella C (2015) Synthesis and characterization of cerium oxide nanoparticles by using rapid precipitation method. *Nanotechnology* 4:91–93
25. Kim SJ, Chung BH (2016) Antioxidant activity of levan coated cerium oxide nanoparticles. *Carbohydr Polym* 150:400–407
26. Sun C, Chen L (2009) Controllable Synthesis of Shuttle-Shaped Ceria and Its Catalytic Properties for CO Oxidation. *Eur J Inorg Chem* 2009:3883–3887
27. Zhang D, Niu F, Li H, Shi L, Fang J (2011) Uniform ceria nanospheres: Solvothermal synthesis, formation mechanism, size-control and catalytic activity. *Powder Technol* 207:35–41
28. Yin L, Wang Y, Pang G, Koltypin Y, Gedanken A (2002) Sonochemical Synthesis of Cerium Oxide Nanoparticles—Effect of Additives and Quantum Size Effect. *J Colloid Interface Sci* 246:78–84
29. Soren S, Jena SR, Samanta L, Parhi P (2015) Antioxidant Potential and Toxicity Study of the Cerium Oxide Nanoparticles Synthesized by Microwave-Mediated Synthesis. *Appl Biochem Biotechnol* 177:148–161
30. Ferreira NS, Angélica RS, Marques VB, deLima CCO, Silva MS (2016) Cassava-starch-assisted sol-gel synthesis of CeO₂ nanoparticles. *Mater Lett* 165:139–142
31. Hedrick JB, Sinha SP (1994) Cerium-based polishing compounds: discovery to manufacture. *J Alloys Compd* 207/208:377–382
32. Masui T, Yamamoto M, Sakata T, Mori H, Adachi G (2000) Synthesis of BN-coated CeO₂ fine powder as a new UV blocking material. *J Mater Chem* 10:353–357
33. Inaba H, Tagawa H (1996) Ceria-based solid electrolytes. *Solid State Ion* 83:1–16
34. Yang J, Peng S, Shi Y, Ma S, Ding H, Rupprechter G, Wang J (2020) Fast Visual Evaluation of the Catalytic Activity of CeO₂: Simple Colorimetric Assay Using 3,3',5,5'-tetramethylbenzidine as

Indicator. *J Catal* 389:71–77

35. Zholobak NM, Ivanov VK, Shcherbakov AB, Shaporev AS, Polezhaeva OS, Baranchikov AY, Spivak NY, Tretyakov YD (2011) UV-shielding property, photocatalytic activity and photocytotoxicity of ceria colloid solutions. *J Photochem Photobiol B Biol* 102:32–38
36. Dao NN, Luu MD, Nguyen QK, Kim BS (2011) UV absorption by cerium oxide nanoparticles/epoxy composite thin films. *Adv Nat Sci Nanosci Nanotechnol* 2:1–4
37. Sujesh G, Ganesan S, Ramesh S (2020) Effect of CeO₂ nano powder as additive in WME-TPO blend to control toxic emissions from a light-duty diesel engine – An experimental study. *Fuel* 278:1–9
38. Huang W, Zhang Y, Li Y, Zeng T, Wan Q, Yang N (2020) Morphology-controlled electrochemical sensing of environmental Cd²⁺ and Pb²⁺ ions on expanded graphite supported CeO₂ nanomaterials. *Anal Chim Acta* 1126:63–71
39. Yuan Q, Duan HH, Li LL, Sun LD, Zhang YW, Yan CH (2009) Controlled synthesis and assembly of ceria-based nanomaterials. *J Colloid Interface Sci* 335:151–167
40. Adachi G, Imanaka N (1998) The Binary Rare Earth Oxides. *Chem Rev* 98:1479–1514
41. Guzman M, Estrada M, Miridonov S, Simakov A (2019) Synthesis of cerium oxide (IV) hollow nanospheres with tunable structure and their performance in the 4-nitrophenol adsorption. *Microporous Mesoporous Mater* 278:241–250
42. Zhao K, Qi J, Zhao S, Tang H, Yin H, Zong L, Chang L, Gao Y, Yu R, Tang Z (2015) Multiple Au cores in CeO₂ hollow spheres for the superior catalytic reduction of p-nitrophenol. *Chinese J Catal* 36:261–267
43. Zhang X, Su L, Kong Y, Ma D, Ran Y, Peng S, Wang L, Wang Y (2020) CeO₂ nanoparticles modified by CuO nanoparticles for low-temperature CO oxidation with high catalytic activity. *J Phys Chem Solids* 147:109651
44. Chen Z, Chen L, Jiang M, Gao X, Huang M, Li Y, Ren L, Yang Y, Yang Z (2020) Controlled synthesis of CeO₂ nanorods and their promotional effect on catalytic activity and aging resistibility for diesel soot oxidation. *Appl Surf Sci* 510:145401
45. Li S, Zhang Y, Wang Z, Du W, Zhu G (2020) Morphological Effect of CeO₂ Catalysts on Their Catalytic Performance in Lean Methane Combustion. *Chem Lett* 49:461–464
46. Tomishige K, Gu Y, Chang T, Tamura M, Nakagawa Y (2020) Catalytic function of CeO₂ in non-reductive conversion of CO₂ with alcohols. *Materials Today Sustainability* 9:100035
47. Kaur A, Singh D, Sud D (2020) A review on grafted, crosslinked and composites of biopolymer Xanthan gum for phasing out synthetic dyes and toxic metal ions from aqueous solutions. *J Polym Res* 27:1–19
48. Pandey S, Ramontja J (2016) Rapid, Facile Microwave-assisted synthesis of Xanthan gum grafted polyaniline for chemical sensor. *Int J Biol Macromol* 89:89–98
49. Garc a-Ochoa F, Santos VE, Casas JA, Go mez E (2000) Xanthan gum: production, recovery, and properties. *Biotechnol Adv* 18:549–579

50. Elella MHA, Sabaa MW, ElHafeez EA, Mohamed RR (2019) Crystal violet dye removal using crosslinked grafted xanthan gum. *Int J Biol Macromol* 137:1086–1101
51. Cai X, Dua X, Cui D, Wang X, Yang Z, Zhu G (2019) Improvement of stability of blueberry anthocyanins by carboxymethyl starch/xanthan gum combinations microencapsulation. *Food Hydrocoll* 91:238–245
52. William JKM, Ponmani S, Samuel R, Nagarajan R, Sangwai JS (2014) Effect of CuO and ZnO nanofluids in xanthan gum on thermal, electrical and high pressure rheology of water-based drilling fluids. *J Pet Sci Eng* 117:15–27
53. Ebrahiminezhad A, Moeeni F, Taghizadeh SM, Seifan M, Bautista C, Novin D, Ghasemi Y, Berenjian A (2019) Xanthan Gum Capped ZnO Microstars as a Promising Dietary Zinc Supplementation. *Foods* 8:1–10
54. Rahdar A, Aliahmad M, Hajinezhad MR, Samani M (2018) Xanthan Gum-stabilized Nano-Ceria: green chemistry based synthesis, characterization, study of biochemical alterations induced by intraperitoneal doses of nanoparticles in Rat. *J Mol Struct* 1173:166–172
55. Loganathan S, Sankaran S (2021) Surface chemical and selective flocculation studies on iron oxide and silica suspensions in the presence of xanthan gum. *Miner Eng* 160:106668
56. Liu TT, Wang MH, Zhang HP, Zhao ZY (2015) Sol–gel synthesis of doped nanocrystalline ZnO powders using xanthan gum and varistor properties study. *J Mater Sci Mater Electron* 26:9056–9062
57. Li T, Deng X, Wang J, Chen Y, He L, Sun Y, Song C, Zhou Z (2014) Biodegradation of nitrobenzene in a lysogeny broth medium by a novel halophilic bacterium *Bacillus licheniformis*. *Mar Pollut Bull* 89:384–389
58. Altenburger R, Schmitt H, Schuurmann G (2005) Algal toxicity of nitrobenzenes: combined effect analysis as a pharmacological probe for similar modes of interaction. *Environ. Toxicol. Chem.* SETAC, USA
59. Burke SD, Danheiser RL (1999) *Handbook of Reagents for Organic Synthesis; Oxidizing and Reducing Agents*. John Wiley and Sons, New York
60. Penne JS (1991) *Reductions by the alumino and borohydrides in organic synthesis*. VCH publishers, New York
61. Aditya T, Jana J, Singh NK, Pal A, Pal T (2017) Remarkable Facet Selective Reduction of 4Nitrophenol by Morphologically Tailored (111) Faceted Cu₂O Nanocatalyst. *ACS Omega* 2:1968–1984
62. Fountoulaki S, Daikopoulou V, Gkizis PL, Tamiolakis I, Armatas GS, Lykakis IN (2014) Mechanistic Studies of the Reduction of Nitroarenes by NaBH₄ or Hydrosilanes Catalyzed by Supported Gold Nanoparticles. *ACS Catal* 4:3504–3511
63. Chiu HY, Afedzi TW, Liu YT, Ghanbari F, Lin KYA (2020) Cobalt Oxides with Various 3D Nanostructured Morphologies for Catalytic Reduction of 4-Nitrophenol: A Comparative Study. *J Water Process Eng* 37:101379

64. Nandanwar SU, Chakraborty M (2012) Synthesis of Colloidal CuO/ γ -Al₂O₃ by Microemulsion and Its Catalytic Reduction of Aromatic Nitro Compounds. *Chin J Catal* 33:1532–1541
65. Alam MK, Rahman MM, Abbas M, Torati SR, Asiri AM, Kim D, Kim C (2017) Ultra-sensitive 2-nitrophenol detection based on reduced graphene oxide/ZnO nanocomposites. *J Electroanal Chem* 78:66–73
66. Yourdkhani A, Caruntu G (2011) Highly ordered transition metal ferrite nanotube arrays synthesized by template-assisted liquid phase deposition. *J Mater Chem* 21:7145–7153
67. Bindu P, Thomas S (2014) Estimation of lattice strain in ZnO nanoparticles: X-ray peak profile analysis. *J Theor Appl Phys* 8:123–134
68. Anbu N, Vijayan C, Dhakshinamoorthy A (2019) A Versatile, Mild and Selective Reduction of Nitroarenes to Aminoarenes Catalyzed by CeO₂ Nanoparticles with Hydrazine Hydrate. *ChemistrySelect* 4:1379–1386
69. Sreeju N, Rufus A, Philip D (2016) Microwave-assisted rapid synthesis of Copper nanoparticles with exceptional stability and their multifaceted application. *J Mol Liq* 221:1008–1021
70. Cai K, Zhou Y (2014) Reduction of Aromatic Nitro Compounds to Azoxy Compounds with Sodium Borohydride. *Adv Mat Res* 1033–1034:18–21
71. Wu W, Lin R, Shen L, Liang R, Yuan R, Wu L (2013) Highly efficient visible-light-induced photocatalytic hydrogenation of nitrobenzene to aniline in water. *RSC Adv* 3:10894–10899
72. Dong J, Zhao Y, Zhao R, Zhou R (2010) Effects of pH and particle size on kinetics of nitrobenzene reduction by zero-valent iron. *J Environ Sci* 22:1741–1747
73. Wu S, Dzubiella J, Kaiser J, Drechsler M, Guo X, Ballauff M, Lu Y (2012) Thermosensitive Au-PNIPAA Yolk–Shell Nanoparticles with Tunable Selectivity for Catalysis. *Angew Chem Int Ed* 51:2229–2233
74. Basu S, Sengupta JK S (2019) Catalytic Reduction of Nitrobenzene Using Silver Nanoparticles Embedded Calcium Alginate Film. *J Nanosci Nanotechnol* 19:7487–7492
75. El-Hout SI, El-Sheikh SM, Hassan HMA, Harraz FA, Ibrahim IA, El-Sharkawy EA (2015) A green chemical route for synthesis of graphene supported palladium nanoparticles: A highly active and recyclable catalyst for reduction of nitrobenzene. *Appl Catal A-Gen* 503:176–185
76. Thawarkar SR, Thombare B, Munde BS, Khupse ND (2018) Kinetic investigation for the catalytic reduction of nitrophenol using ionic liquid stabilized gold nanoparticles. *RSC Adv* 8:38384–38390
77. Zhang X, Qu Y, Shen W, Wang J, Li H, Zhang Z, Li S, Zhou J (2016) Biogenic synthesis of gold nanoparticles by yeast *Magnusiomyces ingens* LH-F1 for catalytic reduction of nitrophenols. *Colloids Surf A Physicochem Eng Asp* 497:280–285
78. Wu C, An X, Gao S, Su L (2015) Self-assembly of cuprous oxide nanoparticles supported on reduced graphene oxide and their enhanced performance for catalytic reduction of nitrophenols. *RSC Adv* 5:71259–71267

Figures

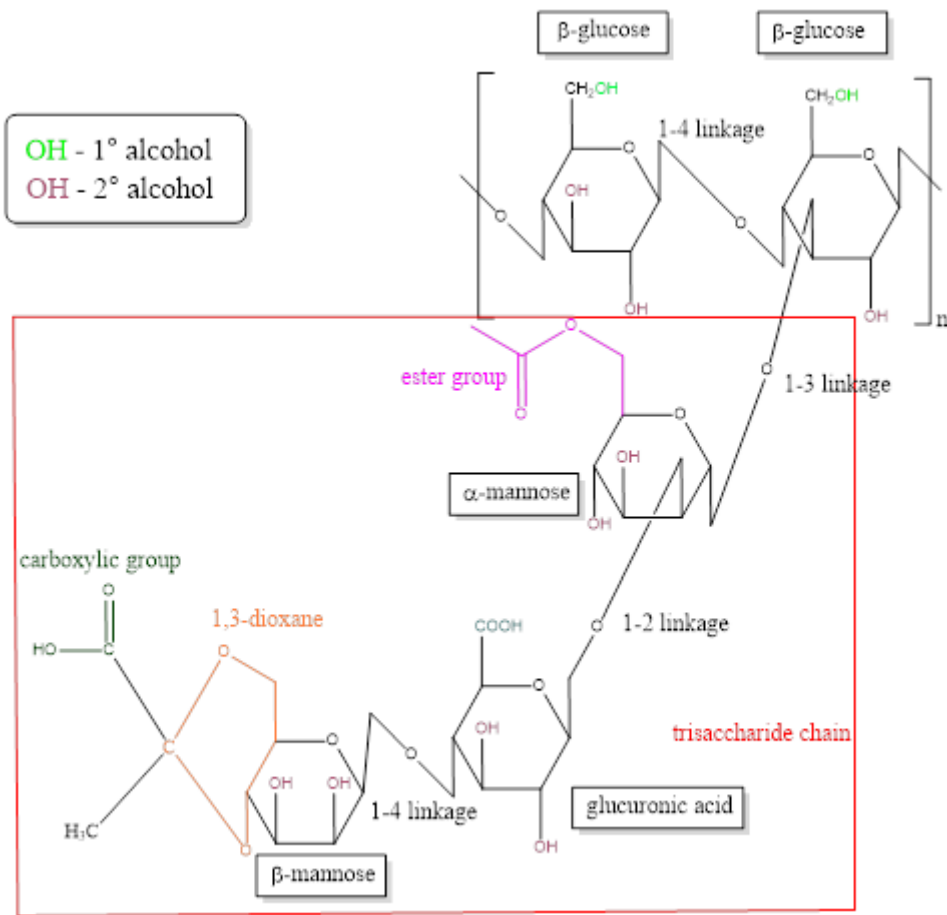


Figure 1

Structure of xanthan gum

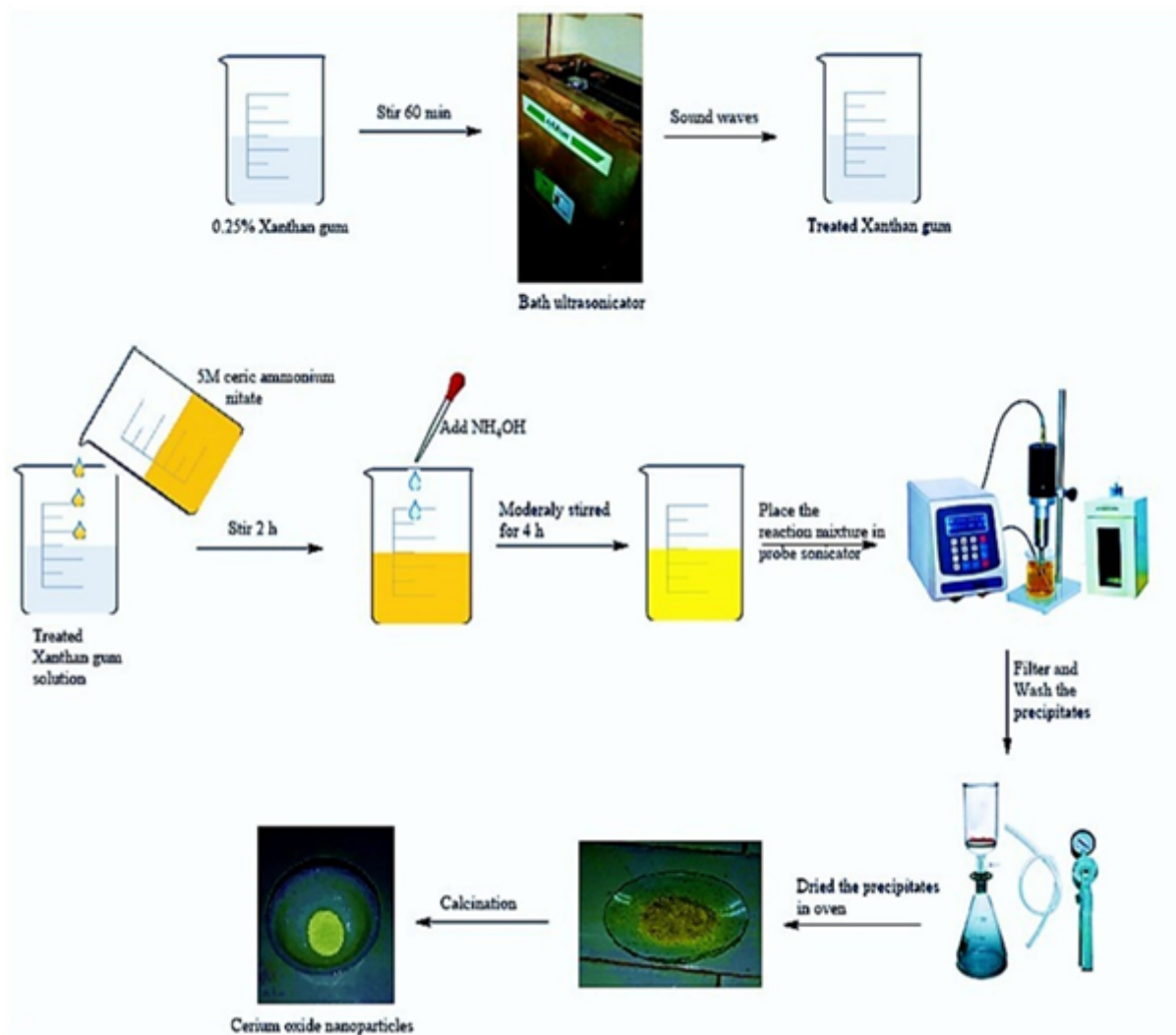


Figure 2

Synthetic scheme of CeO₂ nanoparticles

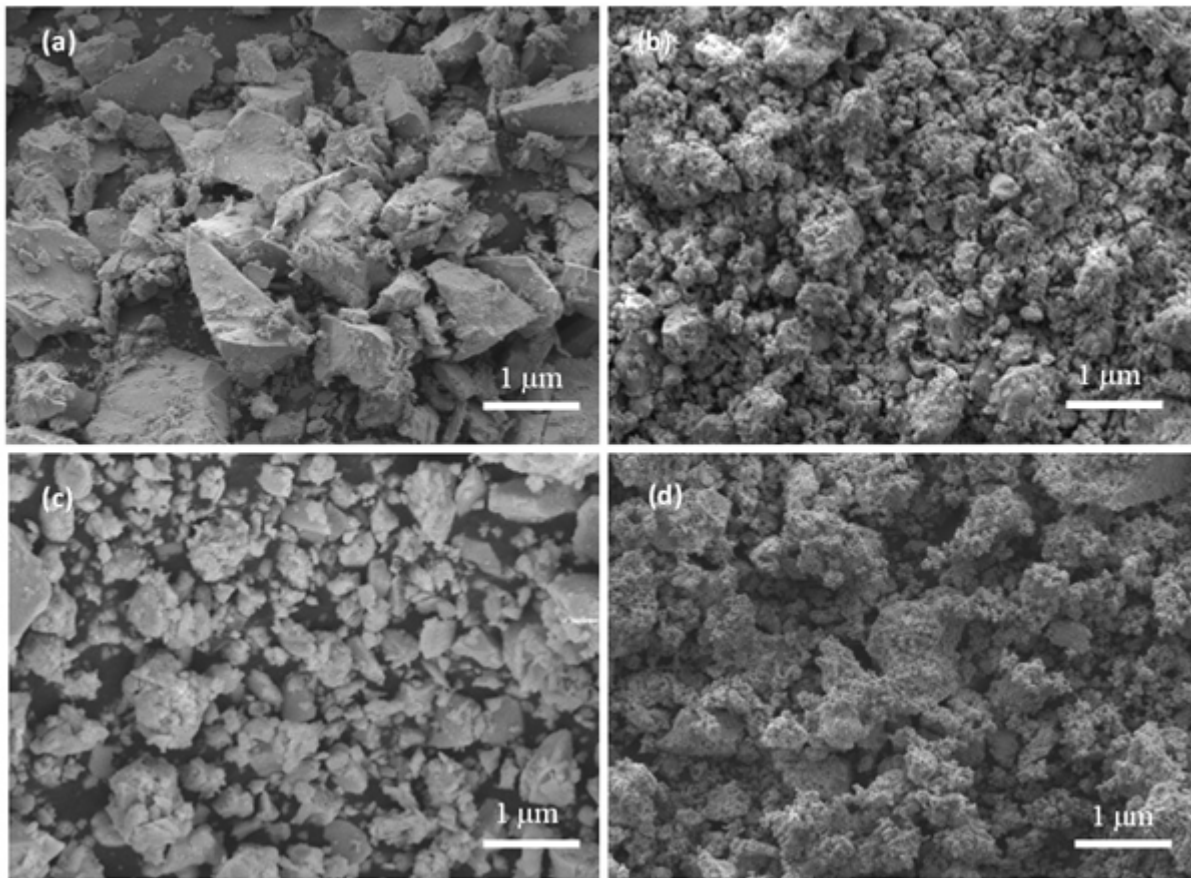


Figure 3

FESEM images of (a) C-350, (b) C-500, (c) C-650, and (d) C-800 CeO₂ nanoparticles

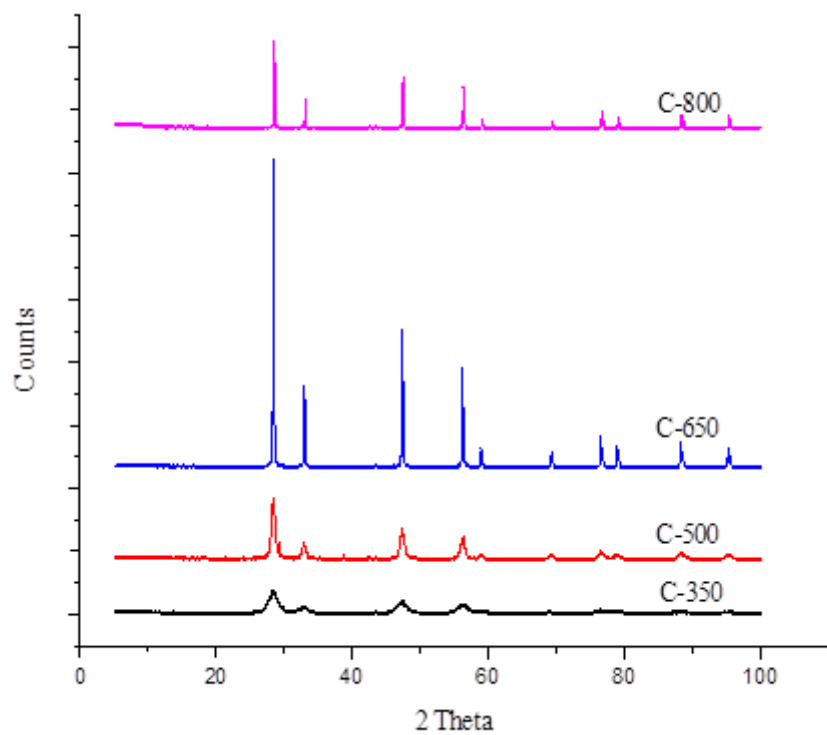


Figure 4

XRD pattern of C-350, C-500, C-650, and C-800 CeO₂ nanoparticles

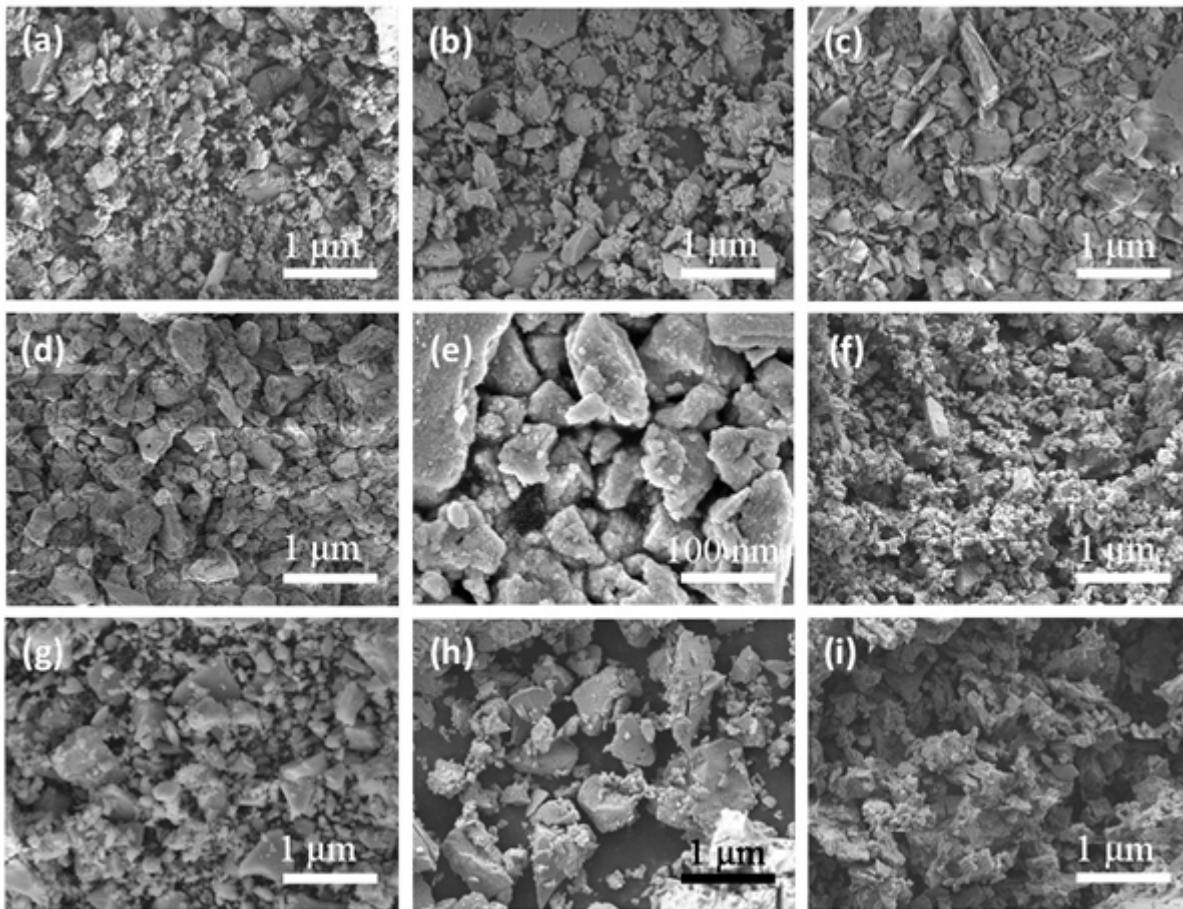


Figure 5

FESEM images illustrate the morphologies of template assisted CeO₂ nanoparticles at (a) 10 min, (b) 15 min, (c) 20 min, (d) 25 min, (e) 30 min, (f) 35 min, (g) 40 min, (h) 45 min and (i) 50 min reaction time

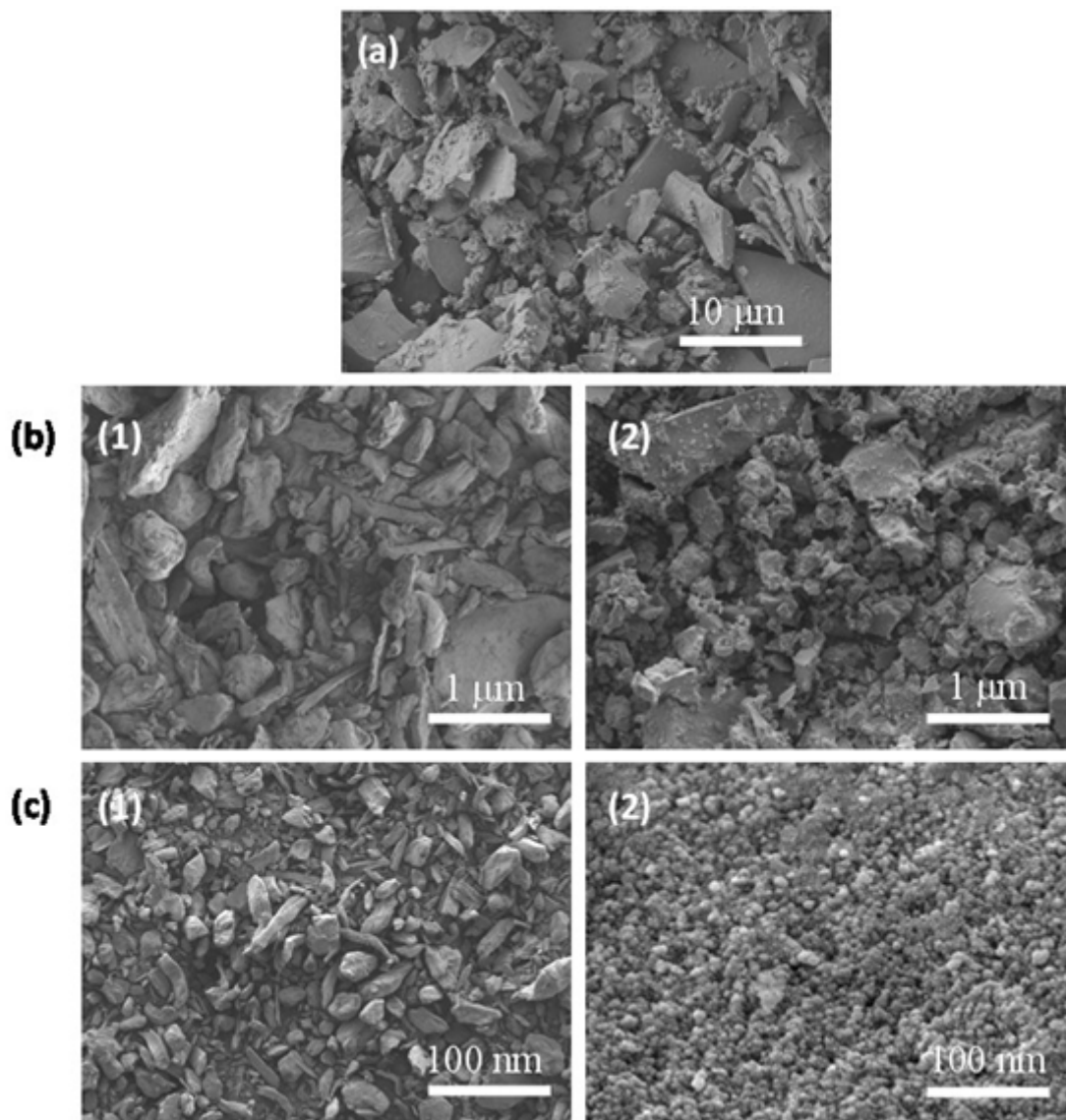


Figure 6

FESEM images of (a) template free CeO₂ nanoparticles (b-1) xanthan gum, (b-2) xanthan gum assisted CeO₂ nanoparticles, (c-1) treated xanthan gum, (c-2) treated xanthan gum assisted CeO₂ nanoparticles

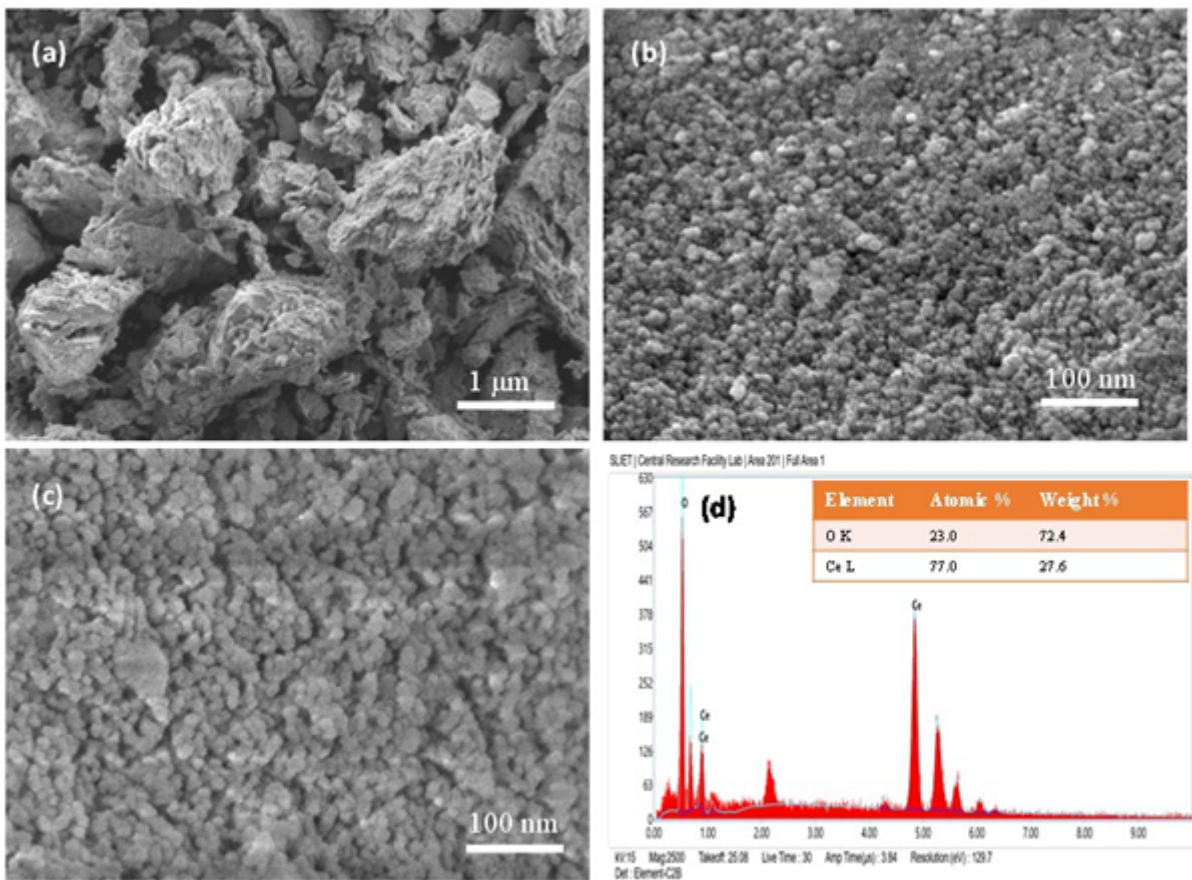


Figure 7

FESEM images of CeO₂ nanoparticles (a) C-20, (b) C-40 and (c) C-60

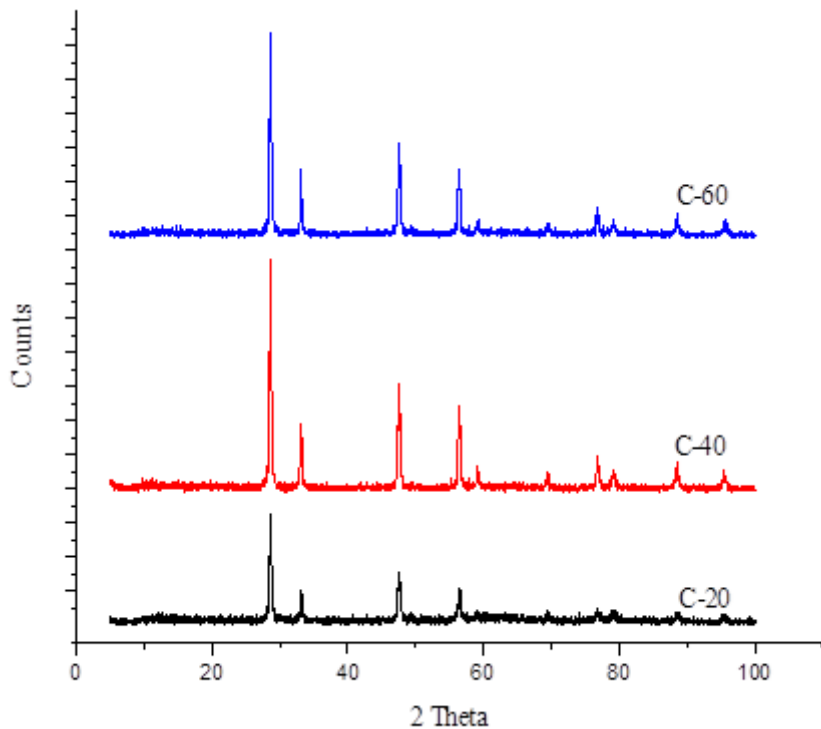


Figure 8

XRD pattern of CeO₂ nanoparticles (C-20, C-40, and C-60)

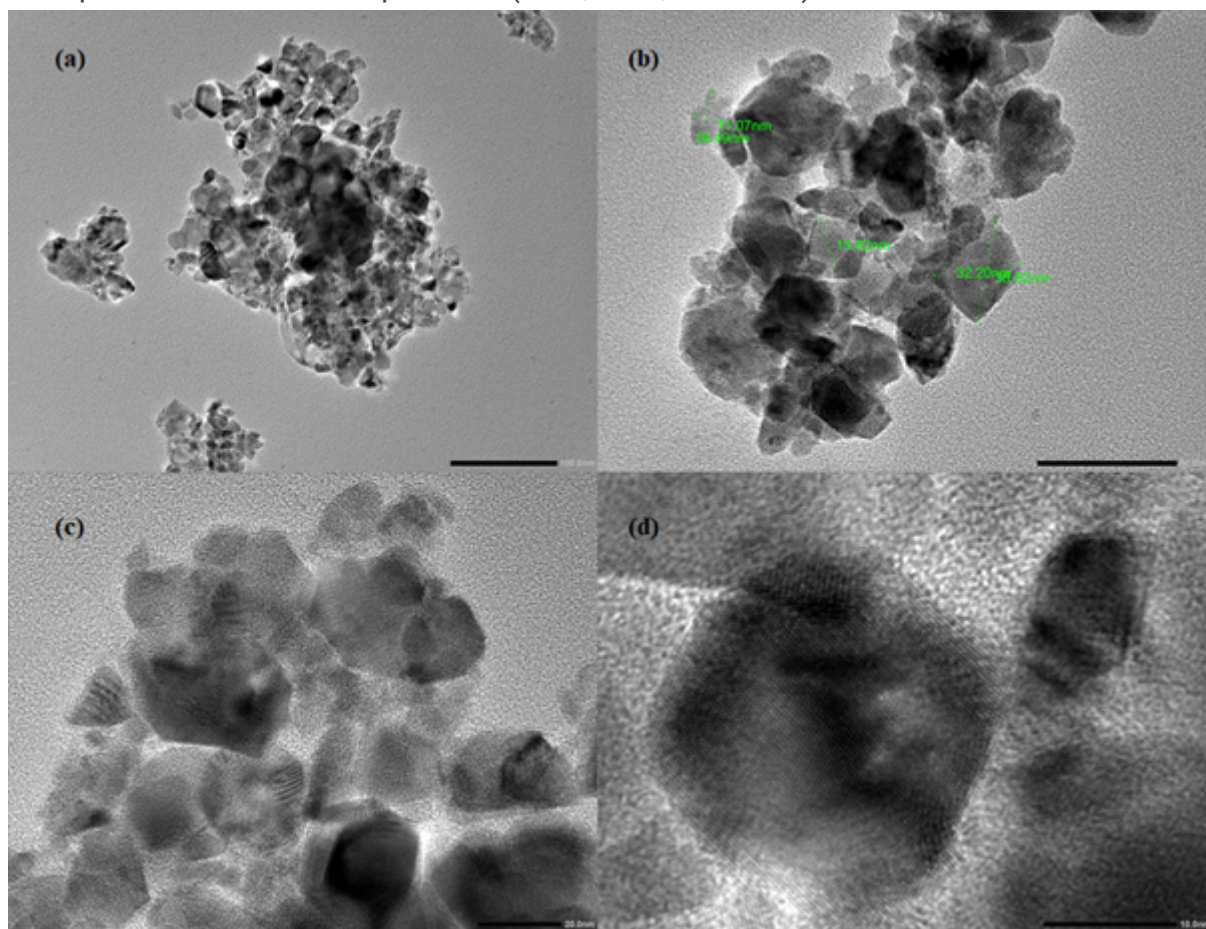


Figure 9

HRTEM images of CeO₂ nanoparticles (C-40 sample) at different magnifications (a) 100 nm (b) 50 nm (c) 20 nm (d) 10 nm

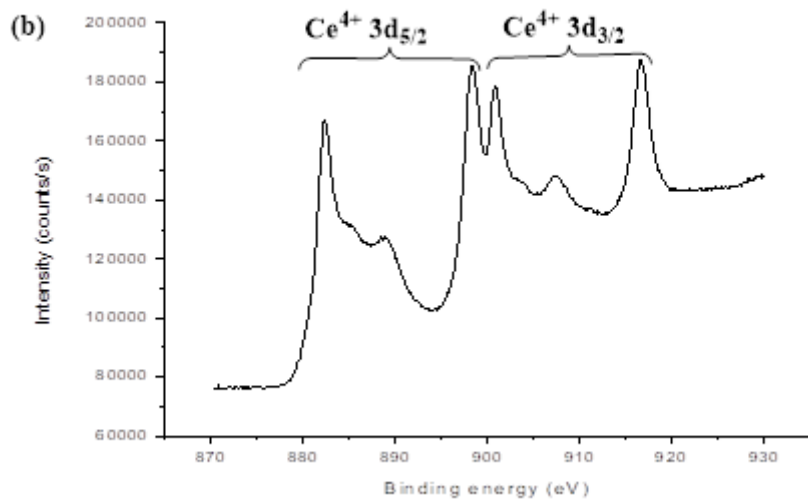
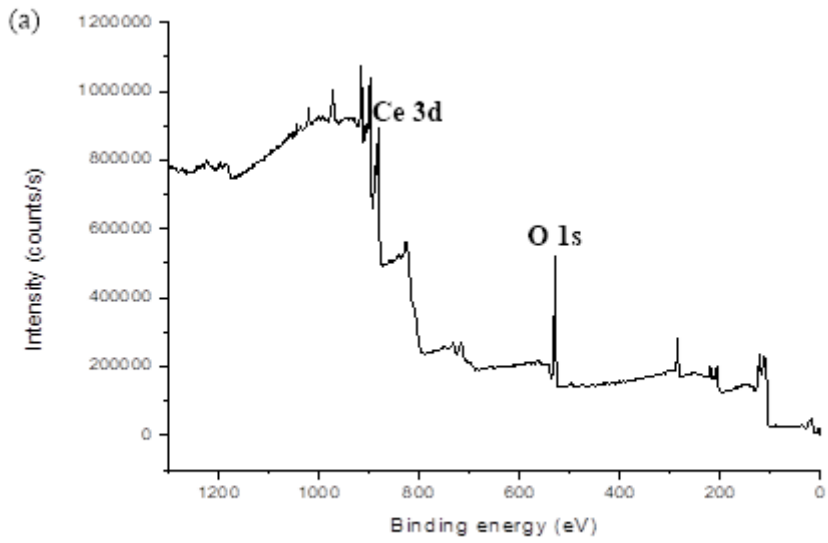


Figure 10

XPS spectra of CeO₂ nanoparticles (C-40)

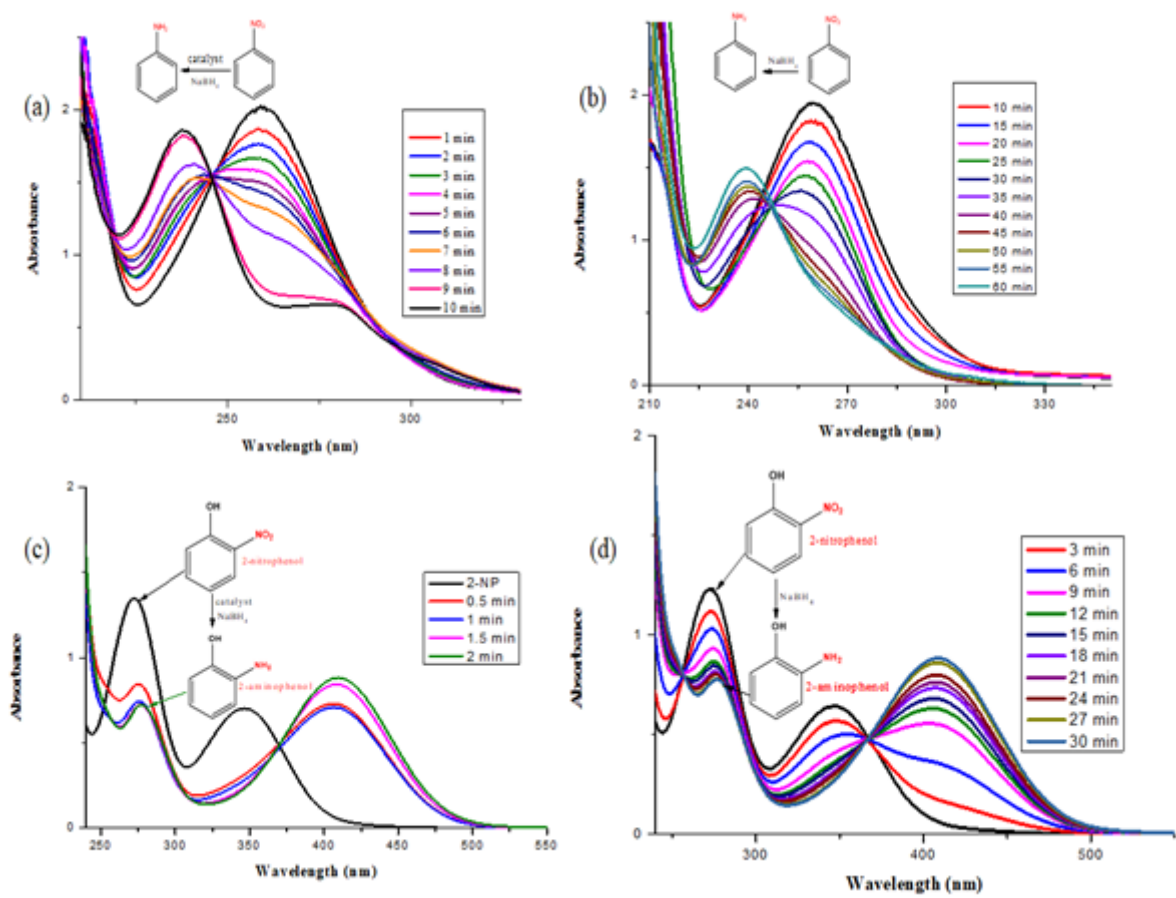


Figure 11

UV-vis absorption spectra of reduction of nitrobenzene (a) in the presence (b) in the absence of catalyst; reduction of 2-nitrophenol (c) in the presence (d) in the absence of the catalyst

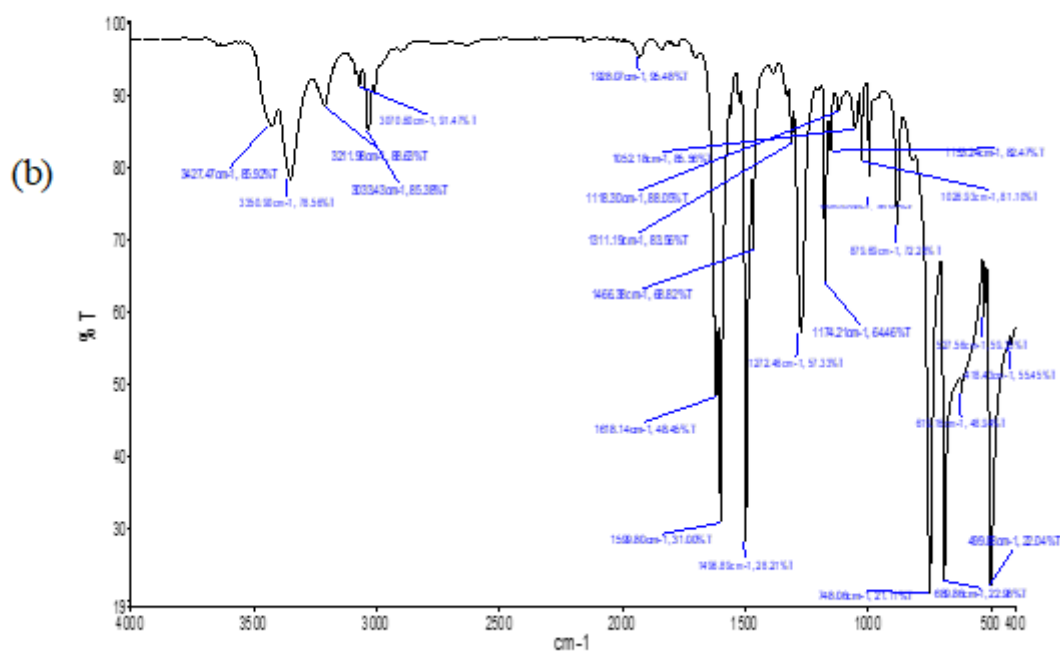
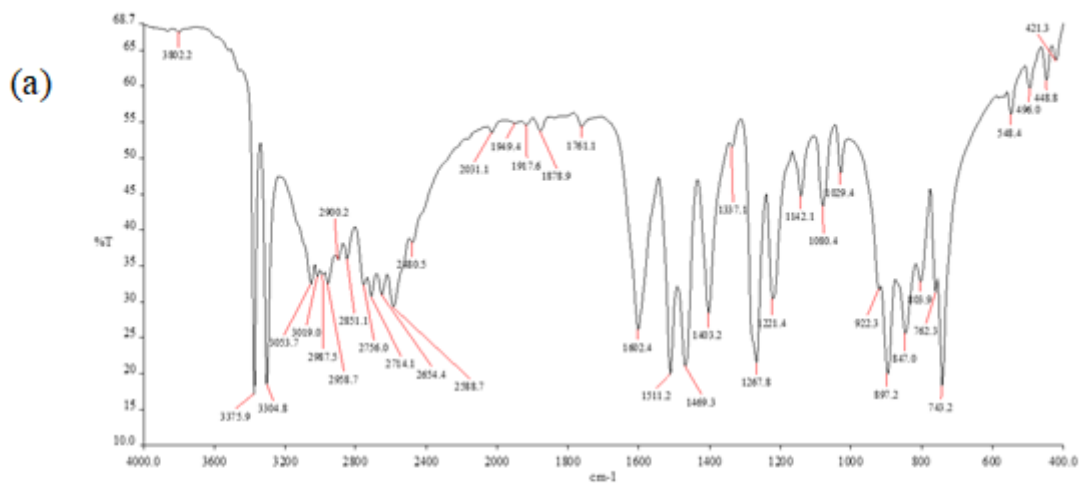


Figure 12

FTIR spectra of (a) 2-aminophenol and (b) aminobenzene or aniline

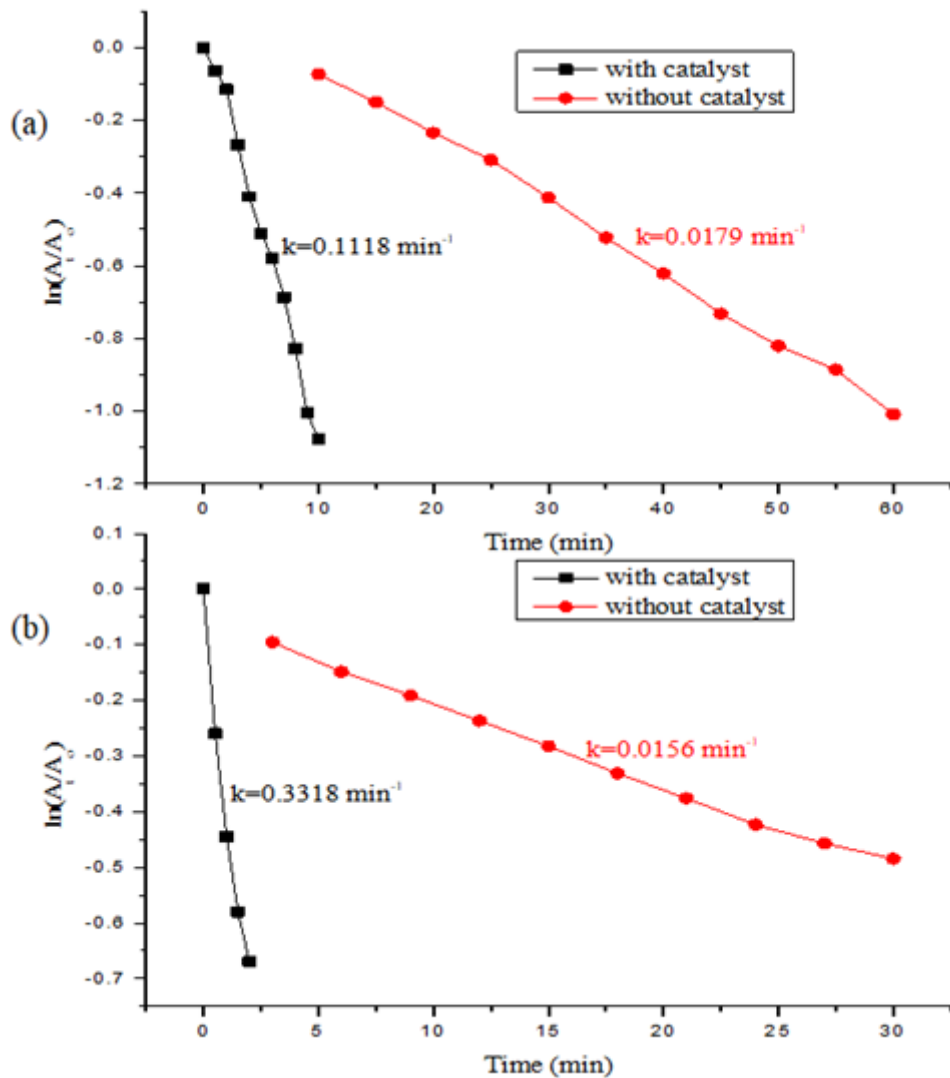


Figure 13

represents the correlation between $\ln(A_t/A_0)$ and time for the reduction of (a) nitrobenzene and (b) 2-nitrophenol

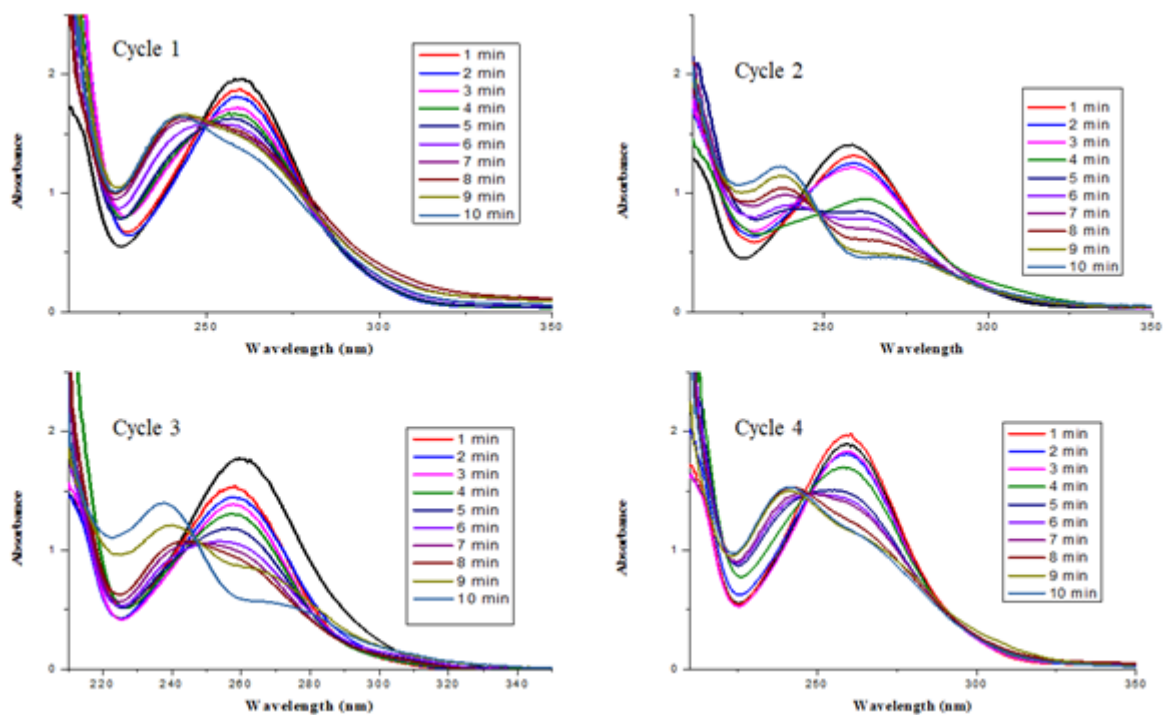


Figure 14

Reusability cycles of the CeO₂ catalyst

Supplementary Files

This is a list of supplementary files associated with this preprint. Click to download.

- [floatimage3.png](#)